PHYSICAL REVIEW A **109**, 022211 (2024)

Boundary criticality of Chern insulator in two-dimensional Su-Schrieffer-Heeger model with next-nearest-neighbor hopping

Kai-Xin Hu,[1] Yu Yan,[1] Zhi-Xu Zhang,[1] Shutian Liu,[1,*] Shou Zhang,[2,†] and Hong-Fu Wang[2,‡]
[1]*School of Physics, Harbin Institute of Technology, Harbin, Heilongjiang 150001, China*
[2]*Department of Physics, College of Science, Yanbian University, Yanji, Jilin 133002, China*

(Received 3 October 2023; accepted 18 January 2024; published 9 February 2024)

We investigate the properties of Chern insulator in a two-dimensional (2D) Su-Schrieffer-Heeger (SSH) model with next-nearest-neighbor (NNN) hopping. We find that the Weyl points, serving as phase-transition points, precisely coincide with high-symmetry points. In the phase diagram, there are two nontrivial phases with different nonzero Chern numbers, one trivial phase with zero Chern number, and two different types of phase-transition boundaries formed by the Weyl points. The system with a nonzero Chern number is topologically nontrivial, with localized edge states at the top and bottom. Interestingly, the eigenmodes on the phase-transition boundaries of two different nontrivial phases are localized at the bottom of the system, in contrast with the extended eigenmodes observed on the trivial and nontrivial phase-transition boundaries. Our work provides insights into exploring the correlation between edge state and phase transition boundary in Chern insulator based on the 2D SSH model with NNN hopping.

DOI: 10.1103/PhysRevA.109.022211

I. INTRODUCTION

The recent development of topological phases in condensed matter has attracted much interest in the research community [1–7]. Many famous lattice models with novel physical properties have been studied, such as the SSH model [8–11], Kitaev model [12–14], Rice-Mele model [15–17], Haldane model [18–20], and Qi-Wu-Zhang model [21–23]. Among these famous topological models, the one-dimensional (1D) SSH model, which has an extremely simple form but rich topological properties, has far-reaching implications for the investigate of condensed-matter physics [24–27]. The 1D SSH model can be extended to a two-dimensional (2D) model [28–30], often referred to as a 2D SSH model. The 2D SSH model is one of the simplest systems for exploring 2D topological systems and has attracted considerable attention in the search for novel topological phases [31–37]. Similar to the 1D SSH model, the 2D SSH model comprises two distinct sublattices within each unit cell. Nevertheless, the 2D SSH model involves a greater number of hopping amplitudes compared with the 1D SSH model. By skillfully manipulating these hopping amplitudes, one can induce topological phase transitions and topological edge states [38–41]. These edge states are important for electron transport and the practical applications of 2D topological insulators [42–47]. Besides, it is crucial to consider the lattice structure and symmetry when studying 2D topological insulators [48–53]. Based on their symmetries, topological systems with and without gaps can be classified [54,55]. One can find the corresponding topological invariants according to the symmetry classification.

The 2D SSH model with nearest-neighbor (NN) hopping amplitudes has received considerable attention in both theoretical and experimental studies [38,56]. However, the influence of next-nearest-neighbor (NNN) hopping amplitudes on the topological phases remains an open question, with less attention given to the 2D SSH model with NNN hopping amplitudes. Recently, topoelectric (TE) circuit networks have emerged as an alternative platform for studying edge states and other topological phenomena [57–60]. The Hamiltonian of these TE circuits can be engineered to emulate the lattice Hamiltonian of condensed-matter systems [61–64]. Unlike material-based platforms, TE circuit networks offer unparalleled control and flexibility in the precise tuning and modulating of coupling coefficients. This is crucial because the flexible selection of these couplings can help us investigate systems with different lattice structure, such as the 2D SSH model with NNN hopping amplitudes.

In this paper, we introduce a 2D SSH model with NN and NNN hopping amplitudes. The primary focus is to investigate the edge states at the topological phase-transition boundary in the 2D SSH model with NN and NNN hopping amplitudes. We propose to achieve the present model by means of topoelectrical (TE) circuit lattice. We show the system undergoes a topological phase transition when the absolute value of the ratio between intracellular and intercellular hopping amplitudes reaches two. By varying the hopping amplitudes, the system undergoes a transition from a normal insulator phase to a Chern insulator phase. The Chern number can serve as the topological invariant that characterizes the topological properties of the 2D SSH model, which becomes nonzero when the intercellular hopping amplitudes are twice as large as the intracellular ones.

The paper is organized as follows: In Sec. II, the 2D SSH model is introduced and the corresponding real-space and Bloch Hamiltonians are given. In Sec. III, we discuss the

---

[*] stliu@hit.edu.cn
[†] szhang@ybu.edu.cn
[‡] hfwang@ybu.edu.cn

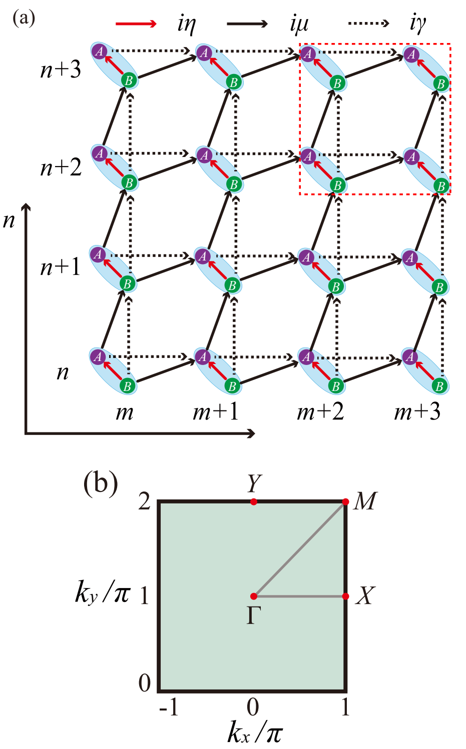

FIG. 1. (a) Schematic diagram of the 2D SSH model with NNN hopping amplitudes. The unit cell is shaded in blue and consisted of sublattice A (purple solid circle) and sublattice B (green solid circle). m (n) represents coordinate in the x (y) direction. The solid red lines represent the intracellular NN hopping amplitudes $i\eta$, solid black lines represent the intercellular NN hopping amplitudes $i\mu$, and black dotted lines represent the intercellular NNN hopping amplitudes $i\gamma$. (b) The first Brillouin zone of the 2D SSH model, where the solid red points represent the high-symmetry points Γ, X, Y, and M.

stripe dispersion relations and topological characterization of the 2D SSH model, and give the spatial distribution of edge states, particularly at the transition boundaries of two different nontrivial phases. In Sec. IV, we discuss the experimental feasibility about 2D SSH model with NN and NNN hopping amplitudes. Finally, a conclusion is given in Sec. V.

II. MODEL AND HAMILTONIAN

The 2D SSH model with NN and NNN hopping amplitudes is shown in Fig. 1(a), where each unit cell is shaded in blue and consists of sublattice A and sublattice B. In real space, the Hamiltonian of the current system is written as

$$\begin{aligned} H = \sum_{\langle m,n\rangle} &(i\eta a^\dagger_{m,n} b_{m,n} + i\mu a^\dagger_{m+1,n} b_{m,n} \\ &+ i\mu b^\dagger_{m,n+1} a_{m,n} + i\gamma a^\dagger_{m+1,n} a_{m,n} \\ &+ i\gamma b^\dagger_{m,n+1} b_{m,n} + \text{H.c.}), \end{aligned} \tag{1}$$

where $a_{m,n}$ and $b_{m,n}$ ($a^\dagger_{m,n}$ and $b^\dagger_{m,n}$) are the annihilation (creation) operators at the $\langle m,n\rangle$th unit cell. The summation of $\langle m,n\rangle$ runs over the unit-cell index. Note that the model includes the intracellular hopping amplitudes $i\eta$, the intercellular NN hopping amplitudes $i\mu$, and the intercellular NNN hopping amplitudes $i\gamma$.

Next, we apply the Fourier transformation $q_{m,n} = \frac{1}{\sqrt{L_x L_y}} \sum_{k_x,k_y} e^{i(k_x mt + k_y nt)} q_{k_x,k_y}$ with $q = a, b$. For simplicity, we take the lattice constant $t = 1$ hereafter. The k_x and k_y are wave vectors defined in the Brillouin region $L_x \times L_y$ of the 2D SSH model. By applying the Fourier transformation, we obtain the Bloch Hamiltonian as

$$H(\mathbf{k}) = \sum_{\mathbf{k}} \psi^\dagger_{\mathbf{k}} \mathcal{H}(\mathbf{k}) \psi_{\mathbf{k}}, \tag{2}$$

where $\psi^\dagger_{\mathbf{k}} = [a^\dagger_{\mathbf{k}}, b^\dagger_{\mathbf{k}}]$ and

$$\mathcal{H}(\mathbf{k}) = \begin{pmatrix} 2\gamma \sin k_x & \Omega \\ \Omega^* & 2\gamma \sin k_y \end{pmatrix}, \tag{3}$$

with $\Omega = i(\eta + \mu e^{-ik_x} - \mu e^{ik_y})$. It can be deduced from $\mathcal{H}^\dagger(\mathbf{k}) = \mathcal{H}(\mathbf{k})$ that the $\mathcal{H}(\mathbf{k})$ is Hermitian. The Bloch Hamiltonian $\mathcal{H}(\mathbf{k})$ has particle-hole symmetry $\hat{C}\mathcal{H}(\mathbf{k})\hat{C}^{-1} = -\mathcal{H}(-\mathbf{k})$ with $\hat{C} = \sigma_0 K$, where σ_0 is the unit matrix and K is the complex conjugation. The Bloch Hamiltonian $\mathcal{H}(\mathbf{k})$ belongs to class D in the tenfold way of Altland-Zirnbauer classification [22,55].

Considering that, in practical systems, the intercellular nearest-neighbor interactions are stronger than the intercellular next-nearest-neighbor interactions, we set $\mu = 2\gamma$ for convenience. By diagonalizing Eq. (3), the energy dispersion can be obtained as

$$\begin{aligned} E(\mathbf{k}) = &\tfrac{1}{2}\mu(\sin k_x + \sin k_y) \pm \tfrac{1}{2}[8\eta\mu(\cos k_x - \cos k_y) \\ &+ 4\eta^2 + \mu^2(8 + 6 \sin k_x \sin k_y + 8 \cos k_y \cos k_x \\ &+ \sin^2 k_x + \sin^2 k_y)]^{\frac{1}{2}}. \end{aligned} \tag{4}$$

The zero-energy condition can be derived from the dispersion relation, allowing one to locate the Weyl points. In this system, there are two bands that exhibit double degeneracy at the Weyl points. The first Brillouin zone (FBZ) of the 2D SSH model is square shaped, whose parameter space is $k_x \in [-\pi, \pi)$ and $k_y \in [0, 2\pi)$, as shown in Fig. 1(b). Four high-symmetry points in the FBZ are $\Gamma = (0, \pi)$, $X = (\pi, \pi)$, $Y = (0, 2\pi)$, and $M = (\pi, 2\pi)$. Through numerical calculations, it is observed that the Weyl points are positioned at the points Γ, $X(Y)$, and M when $\eta/\mu = -2$, 0, and 2, respectively, as shown in Fig. 2. It is noteworthy that the Weyl points that emerge in the BZ correspond to topological phase-transition points. We first examine the condition for the closing of the energy gap, i.e., $E(\mathbf{k}) = 0$. The positions of the Weyl points in the dispersion relation can be determined by the following relations:

$$\begin{aligned} 0 = &\pm i(\sin^2 k_x + \sin^2 k_y + \sin k_x \sin k_y)^{\frac{1}{2}} \\ &+ \cos k_y - \cos k_x - \frac{\eta}{\mu}. \end{aligned} \tag{5}$$

From Eq. (5), we can obtain $\eta/\mu = -2$ when $k_x = 0$ and $k_y = \pi$, indicating the Weyl points located at the high-symmetry points Γ, as shown in Figs. 2(a) and 2(b). For $\eta/\mu = 0$ with $k_x = \pi$ and $k_y = \pi$, we observe the Weyl points at the high-symmetry points X, as depicted in Figs. 2(c) and 2(d). When $\eta/\mu = 2$ with $k_x = \pi$ and $k_y = 2\pi$, Weyl points emerge at the

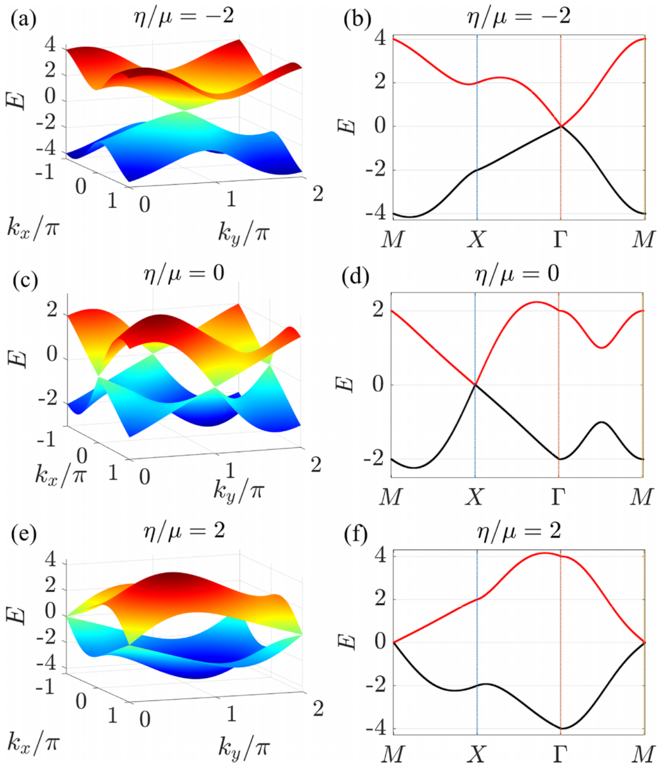

FIG. 2. The bulk dispersion relation of the 2D SSH model for various values of η/μ, with (a) $\eta/\mu = -2$, (c) $\eta/\mu = 0$, (e) $\eta/\mu = 2$. In panels (a), (c), and (e), the bulk gap closes at Weyl points. Band structures along high-symmetry lines of the Hamiltonian $\mathcal{H}(\mathbf{k})$ when (b) $\eta/\mu = -2$, (d) $\eta/\mu = 0$, (f) $\eta/\mu = 2$. In panels (b), (d), and (f), the Weyl points are located at the high-symmetry points M, X, and Γ, respectively.

high-symmetry points M, as shown in Figs. 2(e) and 2(f). Besides, one can find $\eta/\mu = 0$ can also be satisfied when $k_x = \pi$ and $k_y = \pi$, i.e., the Weyl point lies at the high-symmetry point Y. This means there are two Weyl points in the FBZ when $\eta/\mu = 0$, which appear in X and Y points, respectively. But when $\eta/\mu = 2$ (or -2), there is only one Weyl point in the FBZ, which appears in M (or Γ) point. Note that $\eta/\mu = -2$ and $\eta/\mu = 2$ represent the phase-transition boundaries between the topologically trivial and topologically nontrivial phases, whereas $\eta/\mu = 0$ represents the transition boundary between two different topologically nontrivial phases. The band gap closes at the phase transition boundary. For other cases, the two energy bands are gapped. To illustrate more intuitively, we present two gapped cases for $\eta/\mu = -1$ and $\eta/\mu = 1$, as shown in Figs. 3(a) and 3(b), respectively. The topological properties of these two gapped cases will be discussed in detail below.

III. EDGE STATES AND TOPOLOGICAL PHASE TRANSITION

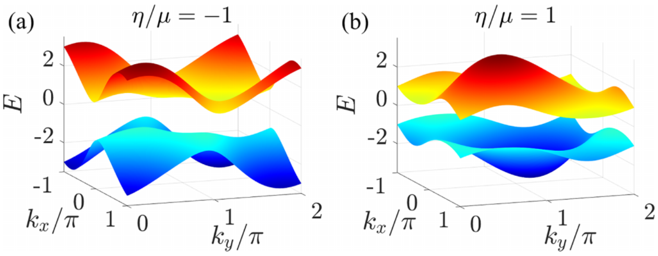

FIG. 3. The bulk dispersion relation of the 2D SSH model for various values of η/μ, with (a) $\eta/\mu = -1$, (b) $\eta/\mu = 1$. Both cases exhibit band gaps in their bulk dispersion relations.

To explore the edge states and the topological phase transition of the system, we investigate the energy-band structures of the strip sample. These band structures can be obtained by solving the Hamiltonian H with open boundary conditions (OBCs) along the y direction and periodic boundary conditions (PBCs) along the x direction. The original Hamiltonian H can be decomposed into a set of 1D lattice Hamiltonians $H(k_x)$ indexed by a continuous parameter k_x, where k_x represents the wave number along the x direction. The resulting k_x-dependent Hamiltonian is given by

$$\begin{aligned} H(k_x) = \sum_{\langle n\rangle}[& i\gamma e^{-ik_x}a_n^\dagger a_n + (i\eta + i\mu e^{-ik_x})a_n^\dagger b_n \\ & + i\mu b_{n+1}^\dagger a_n + i\gamma b_{n+1}^\dagger b_n + \text{H.c.}]. \end{aligned} \tag{6}$$

The inverse participation ratio (IPR) has been widely employed to quantify the localization of states [65], which can be expressed as follows:

$$\mathrm{IPR}(\psi^{(j)}) = \frac{\sum_{n=1}^{2L_y}\left|\psi_n^{(j)}\right|^4}{\left(\sum_{n=1}^{2L_y}\left|\psi_n^{(j)}\right|^2\right)^2}, \tag{7}$$

where $\psi_n^{(j)}$ represents the jth eigenstate, and n denotes the lattice site. For the extended states $\psi^{(j)}$, the IPR $\to 0$, while for the localized states, the IPR $\to 1$. In this context, we introduce the directional IPR (DIPR), as below [66],

$$\mathrm{DIPR}(\psi^{(j)}) = \mathrm{sgn}\left[\sum_{n=1}^{2L_y}(n - L_y - \delta)\left|\psi_n^{(j)}\right|\right]\mathrm{IPR}(\psi^{(j)}), \tag{8}$$

where δ is a positive value and is normally set to be $0 < \delta < 0.5$. For simplicity, we set $\delta = 0.03$. The function sgn(x) returns 1 for positive arguments $x > 0$, -1 for negative arguments $x < 0$, and 0 for argument $x = 0$. Compared with the IPR, the DIPR can determine whether the eigenstate is localized at the top or bottom boundary of the lattice for systems with the OPC along the y direction and the PBC along the x direction. The DIPR takes a positive value when $\psi^{(j)}$ is localized at the top, while it becomes negative when $\psi^{(j)}$ is localized at the bottom. If DIPR $\to 0$, it indicates that the state is extended.

Based on the above analysis, it is worth noting that the edge states connecting the lower and upper bands cross the bulk gap, as shown in Fig. 4. These edge states are characterized by a nonzero DIPR value and are prominently highlighted by the color bar. A pair of edge states emerge at different values of k_x, with their DIPR values approaching $+1$ and -1. This phenomenon is observed in two different topologically nontrivial phases when $\eta/\mu = -1$ and $\eta/\mu = 1$, as depicted in Figs. 4(a) and 4(c). For the phase-transition boundary between two different topologically nontrivial phases, i.e., $\eta/\mu = 0$, the edge states still exist, and the DIPR $\to -0.5$,

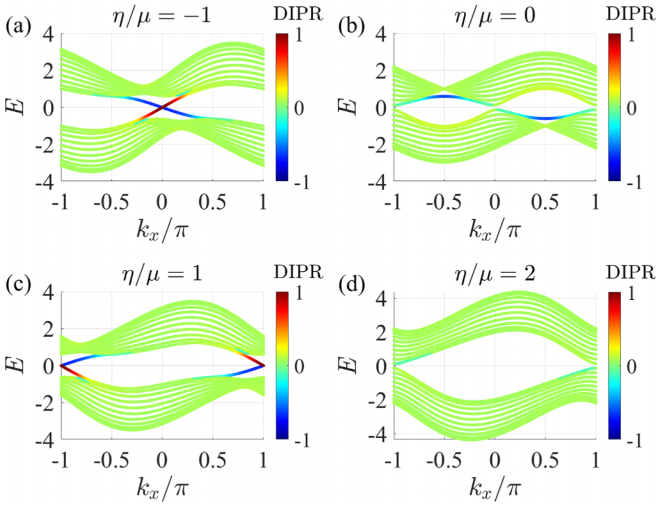

FIG. 4. Stripe dispersion relations of the 2D SSH model along x direction with the stripe width $L_y = 10$ for (a) $\eta/\mu = -1$, (b) $\eta/\mu = 0$, (c) $\eta/\mu = 1$, (d) $\eta/\mu = 2$. The color bar indicates the values of the DIPR. For the topologically nontrivial phase, edge states naturally appear with the DIPR $\neq 0$. The edge states exist in panels (a)–(c), and no edge states are found in panel (d).

as shown in Fig. 4(b). This implies that the eigenmodes at the phase-transition boundary between two topologically nontrivial phases with different Chern numbers become localized. However, there are no edge states for the phase-transition boundary between the topologically trivial and topologically nontrivial phases, i.e., $\eta/\mu = \pm 2$, as shown in Fig. 4(d). Hence, the eigenmodes at the phase-transition boundary between the topologically trivial and topologically nontrivial phases remain extended. Note that the result of our discussion is equally applicable to OBCs along the x direction and PBCs along the y direction.

Next, we investigate the spatial distribution of edge states under different parameter conditions. The energy spectra of the finite system are shown in Figs. 5(a) and 5(c), and the eigenvalues of the edge states in the energy spectra are marked by the dotted red ellipses. The spatial distributions of these edge states are depicted in Figs. 5(b) and 5(d). The highest values of the spatial distributions are observed around the top ($n = N$) and bottom ($n = 1$), which corresponds to the edge state. These edge states with zero energy are distributed at the top and bottom of the system when $\eta/\mu = 1$ and $k_x = \pi$, as shown in Fig. 5(b). However, when $\eta/\mu = 0$ and $k_x = \pi/2$, these edge states deviate from zero energy and are only located at the bottom of the system, as shown in Fig. 5(d).

To characterize the topological properties of the system, we proceed to discuss the topological invariants. In Fig. 3, each band is separated from the other bands by an energy gap. Therefore, the Chern number can serves as the topological invariant that characterizes the topological properties of the 2D SSH system [22,67]. For the two energy bands, the upper and lower bands are denoted by the subscripts + and −, respectively. The energy bands and their corresponding wave functions can be obtained from the Bloch Hamiltonian $\mathcal{H}(\mathbf{k})$, satisfying the Schrödinger equation

$$\mathcal{H}(\mathbf{k})|\psi_{\pm}(\mathbf{k})\rangle = E_{\pm}(\mathbf{k})|\psi_{\pm}(\mathbf{k})\rangle. \tag{9}$$

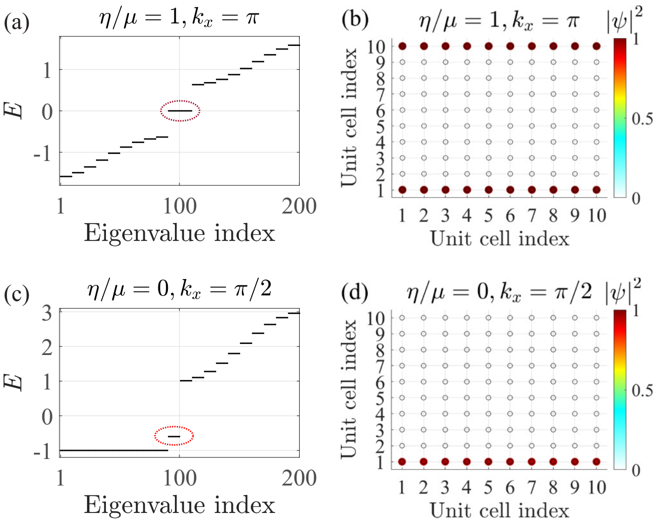

FIG. 5. Energy spectra of the finite system with 10 × 10 unit cells, where (a) $\eta/\mu = 1$ and $k_x = \pi$, (c) $\eta/\mu = 0$ and $k_x = \pi/2$. The eigenvalues of the edge states are marked by the dotted red ellipses. The spatial distribution of the edge states, where (b) $\eta/\mu = 1$ and $k_x = \pi$, (d) $\eta/\mu = 0$ and $k_x = \pi/2$.

The Chern numbers of the two energy bands are given by

$$\mathcal{C}_{\pm} = \frac{1}{2\pi}\int_{\mathrm{BZ}} dk_x dk_y \left(\frac{\partial A_y^{(\pm)}}{\partial k_x} - \frac{\partial A_x^{(\pm)}}{\partial k_y}\right), \tag{10}$$

where the Berry connection is defined as

$$A_j^{(\pm)}(\mathbf{k}) = -i\langle\psi_{\pm}(\mathbf{k})|\partial_{k_j}|\psi_{\pm}(\mathbf{k})\rangle, \quad j = x, y. \tag{11}$$

The Chern numbers of the two energy bands satisfy $\mathcal{C}_+ + \mathcal{C}_- = 0$, where we denote $\mathcal{C} = (\mathcal{C}_+ - \mathcal{C}_-)/2$ for convenience. In the general case, the Chern numbers appear as $\mathcal{C} = 0, \pm 1$. The nonzero Chern number indicates that the system holds a topologically nontrivial phase with two edge states localized at the boundary of the system. The system with a zero Chern number has a topologically trivial phase, implying that no edge states exist in the system.

The Chern numbers $\mathcal{C}$ of the 2D SSH model with NNN hopping as a function of $\eta/|\mu|$, as shown in Fig. 6(a), which

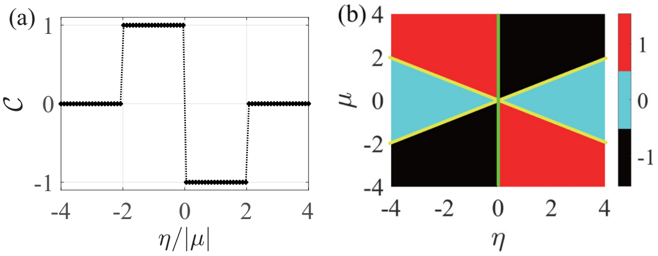

FIG. 6. (a) Chern number $\mathcal{C}$ as a function of $\eta/|\mu|$. (b) The phase diagram of $\mathcal{C}$ on the μ-η plane. The cyan regions represent the trivial phase with $\mathcal{C} = 0$, while the red and black regions represent the topologically nontrivial phase with $\mathcal{C} = +1$ and $\mathcal{C} = -1$, respectively. The boundaries of different regions are marked by gold and green lines, respectively. The color bar indicates the values of the Chern number.

can be expressed as

$$\begin{aligned} \frac{\eta}{|\mu|} &< -2 : \mathcal{C} = 0, \\ -2 < \frac{\eta}{|\mu|} &< 0 : \mathcal{C} = +1, \\ 0 < \frac{\eta}{|\mu|} &< 2 : \mathcal{C} = -1, \\ 2 < \frac{\eta}{|\mu|} &: \mathcal{C} = 0. \end{aligned} \tag{12}$$

The phase diagram of Chern number $\mathcal{C}$ as a function of η and μ is shown in Fig. 6(b). The Chern number $\mathcal{C} = +1$ and $\mathcal{C} = -1$ are located in the red and black regions, respectively. The Chern number $\mathcal{C} = 0$ is located in the cyan regions. The phase-transition boundaries $\eta/|\mu| = \pm 2$ between the topologically trivial phases with $\mathcal{C} = 0$ and topologically nontrivial phases with $\mathcal{C} = \pm 1$ are marked by the gold solid lines. Additionally, the phase-transition boundary $\eta/\mu = 0$ between two different topologically nontrivial phases with $\mathcal{C} = +1$ and $\mathcal{C} = -1$ is marked by the green solid line.

IV. EXPERIMENTAL IMPLEMENTATION

Before the conclusion, we now give a brief discussion about the experimental feasibility. The TE circuits have been extensively investigated both theoretically and experimentally due to their inherent flexibility and tunability, form an ideal platform for implementing various emerging fields such as Chern insulators [63,68], Weyl semimetals [57,58,62], and three-dimensional topological systems [69,70]. Especially the 2D TE Chern circuit that breaks reciprocity via a negative impedance converter (NIC) [63]. Hence, the 2D SSH model with NN and NNN hopping amplitudes shown in Fig. 1(a) can be mapped using TE circuit composed of capacitors and operational amplifiers (op-amps), as shown in Fig. 7(a). The nodes in our TE model is connected with op-amps and capacitance. The grounding mechanism for each electrical node is shown in Fig. 7(b), where all nodes are connected to ground by a capacitance C_1 and common capacitance C. The op-amps are used to obtain nonreciprocal directional coupling between the nodes. The nonreciprocal couplings in the two opposite hopping directions have the same magnitude but a phase difference of π between them. This can be readily implemented by using op-amp-based NIC with current inversion, as shown in Fig. 7(c). This NIC would realize a directional antiphase (π phase difference) coupling between two nodes, i.e., $C_{p,q} = -C_{q,p}$.

Now we show the detailed derivation of Eq. (1). The voltages at the nodes in an electrical network are related by Kirchhoff's current law, which states that the net current flowing in or out of a node is zero. At the A and B node at unit cell $\langle m, n\rangle$, we have

$$\begin{aligned} I^A_{m,n} = &-C_3\frac{d}{dt}\left(V^A_{m,n} - V^A_{m+1,n}\right) + C_3\frac{d}{dt}\left(V^A_{m,n} - V^A_{m-1,n}\right) \\ &+ C_1\frac{d}{dt}\left(V^A_{m,n} - V^B_{m,n}\right) - C_2\frac{d}{dt}\left(V^A_{m,n} - V^B_{m,n+1}\right) \\ &+ C_2\frac{d}{dt}\left(V^A_{m,n} - V^B_{m-1,n}\right) + (C - C_1)\frac{d}{dt}V^A_{m,n} = 0, \end{aligned}$$

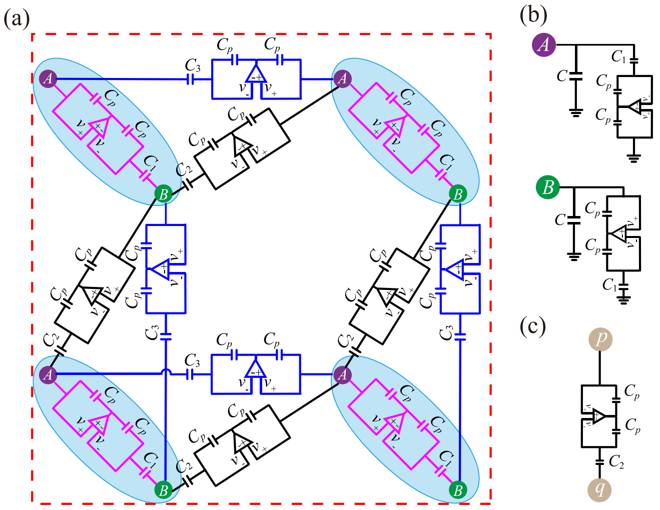

FIG. 7. (a) Illustration of the TE circuit realization. (b) Grounding mechanism of electrical nodes. The common capacitance C plays the role of the TB eigenenergy in the TE equivalent of the Hamiltonian. (c) The elementary unit consisting of op-amp that gives rise to the π-phase difference directional coupling via negative impedance converter with current inversion. The op-amp has a unity gain factor with virtually shorted positive (v_+) and negative (v_-) input terminals. No current flows between v_+ and v_-, so $C_{p,q} = C_2$ and $C_{q,p} = -C_2$.

$$\begin{aligned} I^B_{m,n} = &-C_3\frac{d}{dt}\left(V^B_{m,n} - V^B_{m,n+1}\right) + C_3\frac{d}{dt}\left(V^B_{m,n} - V^B_{m,n-1}\right) \\ &- C_1\frac{d}{dt}\left(V^B_{m,n} - V^A_{m,n}\right) - C_2\frac{d}{dt}\left(V^B_{m,n} - V^A_{m+1,n}\right) \\ &+ C_2\frac{d}{dt}\left(V^B_{m,n} - V^A_{m,n-1}\right) + (C + C_1)\frac{d}{dt}V^B_{m,n} = 0, \end{aligned} \tag{13}$$

where C is the common grounding capacitance, and V^A and V^B are the node voltages at the A and B nodes, respectively. Assume an alternating current flow with an $\exp(i\omega t)$ time dependence. Equation (13) can be cast into the form of

$$\begin{aligned} iCV^A_{m,n} &= iC_1V^B_{m,n} - iC_2\left(V^B_{m,n+1} - V^B_{m-1,n}\right) \\ &\quad - iC_3\left(V^A_{m+1,n} - V^A_{m-1,n}\right), \\ iCV^B_{m,n} &= -iC_1V^A_{m,n} + iC_2\left(V^A_{m,n-1} - V^A_{m+1,n}\right) \\ &\quad - iC_3\left(V^B_{m,n+1} - V^B_{m,n-1}\right). \end{aligned} \tag{14}$$

Applying Eq. (14) at all the voltage nodes, the resulting set of equations can be written as

$$iC\boldsymbol{V} = \boldsymbol{H}\boldsymbol{V}, \tag{15}$$

where $\boldsymbol{V} = [V^A_{1,1}, V^B_{1,1}, V^A_{1,2}, \ldots, V^B_{m,n-1}, V^A_{m,n}, V^B_{m,n}]^T$ is the column vector of the node voltages, and $\boldsymbol{H}$ is the matrix formed by the elements on the right-hand side of Eq. (15), which can be written as

$$
\begin{aligned}
\boldsymbol{H} = \sum_{\langle m,n\rangle} \big(& iC_1 V^{A\dagger}_{m,n} V^{B}_{m,n} - iC_1 V^{A}_{m,n} V^{B\dagger}_{m,n} \\
& - iC_2 V^{A\dagger}_{m,n} V^{B}_{m,n+1} + iC_2 V^{A}_{m,n-1} V^{B\dagger}_{m,n} \\
& + iC_2 V^{B}_{m-1,n} V^{A\dagger}_{m,n} - iC_2 V^{B\dagger}_{m,n} V^{A}_{m+1,n} \\
& - iC_3 V^{A\dagger}_{m,n} V^{A}_{m+1,n} + iC_3 V^{A\dagger}_{m,n} V^{A}_{m-1,n} \\
& - iC_3 V^{B\dagger}_{m,n} V^{B}_{m,n+1} + iC_3 V^{B\dagger}_{m,n} V^{B}_{m,n-1} \big). \qquad (16)
\end{aligned}
$$

We can find Eq. (15) is the TE equivalent of the Schrödinger equation $E\psi = H\psi$, where iC and $\boldsymbol{V}$ play the roles of the energy eigenvalue E and eigenfunction ψ, respectively. Afterward, the Eq. (16) can be mapped to the tight-binding lattice Hamiltonian H as follows:

$$
\begin{aligned}
H = \sum_{\langle m,n\rangle} (& iC_1 a_{m,n} b^{\dagger}_{m,n} - iC_2 a^{\dagger}_{m,n} b_{m,n+1} \\
& - iC_2 b^{\dagger}_{m,n} a_{m+1,n} - iC_3 a^{\dagger}_{m,n} a_{m+1,n} \\
& - iC_3 b^{\dagger}_{m,n} b_{m,n+1} + \text{H.c.}). \qquad (17)
\end{aligned}
$$

For simplicity, we set $C_1 = \eta$, $C_2 = \mu$, and $C_3 = \gamma$, then we can get the final effective Hamiltonian (1). Using the above methods, we can use TE circuit to investigate the 2D SSH model with NN and NNN hopping and find novel topological properties at the phase-transition boundary.

V. CONCLUSIONS

In conclusion, we have investigated the criticality of phase-transition boundary in a 2D SSH model with NNN hopping. The system exhibits a topologically nontrivial phase with zero-energy edge states located at the top and bottom of the system, and has nonzero Chern number. Notably, the Weyl points occur exactly at the high-symmetry points, forming phase-transition boundaries, and have zero Chern number. Our work reveals the criticality of the phase-transition boundary. In contrast with the absence of edge states at the transition boundary of trivial and nontrivial phases, edge states are present at the transition boundary of two different topologically nontrivial phases. Unlike the zero-energy edge states that are located at both ends of the system which exist in topologically nontrivial phases, the edge states on the phase-transition boundary of the two different nontrivial phases deviate from zero energy and are exclusively located at the bottom end of the system. Furthermore, we also discuss the possible way of implementing the present model in 2D nonreciprocal TE circuit lattice.

ACKNOWLEDGMENTS

This work was supported by the National Natural Science Foundation of China under Grants No. 12375020, No. 12074330, No. 62071412, and No. 12074094.

---

[1] J. M. Hou and W. Chen, Phys. Rev. A **93**, 063626 (2016).

[2] H. Wu and J. H. An, Phys. Rev. B **102**, 041119(R) (2020).

[3] X. W. Xu, Y. Z. Li, Z. F. Liu, and A. X. Chen, Phys. Rev. A **101**, 063839 (2020).

[4] A. Yoshida, Y. Otaki, R. Otaki, and T. Fukui, Phys. Rev. B **100**, 125125 (2019).

[5] G. G. Pyrialakos, H. Z. Ren, P. S. Jung, M. Khajavikhan, and D. N. Christodoulides, Phys. Rev. Lett. **128**, 213901 (2022).

[6] W. Chen, S. Cheng, J. Lin, R. Asgari, and G. Xianlong, Phys. Rev. B **106**, 144208 (2022).

[7] L. Qi, A. L. He, H. F. Wang, and Y. J. Liu, Phys. Rev. B **107**, 115107 (2023).

[8] A. J. Heeger, S. Kivelson, J. R. Schrieffer, and W. P. Su, Rev. Mod. Phys. **60**, 781 (1988).

[9] Z. X. Zhang, R. Huang, L. Qi, Y. Xing, Z. J. Zhang, and H. F. Wang, Ann. Phys. (Berlin, Ger.) **533**, 2000272 (2020).

[10] Z. Oztas and N. Candemir, Phys. Lett. A **383**, 1821 (2019).

[11] L. N. Zheng, X. X. Yi, and H. F. Wang, Phys. Rev. Appl. **18**, 054037 (2022).

[12] S. Okamoto, Phys. Rev. B **87**, 064508 (2013).

[13] X. Wang, T. Liu, Y. Xiong, and P. Tong, Phys. Rev. A **92**, 012116 (2015).

[14] Y. Yan, L. Qi, D. Y. Wang, Y. Xing, H. F. Wang, and S. Zhang, Ann. Phys. (Berlin, Ger.) **532**, 1900479 (2020).

[15] M. J. Rice, Y. R. Wang, and E. J. Mele, Phys. Rev. B **40**, 5304 (1989).

[16] K. Hattori, K. Ishikawa, and Y. Kaneko, Phys. Rev. B **107**, 115401 (2023).

[17] A. Przysiężna, O. Dutta, and J. Zakrzewski, New J. Phys. **17**, 013018 (2015).

[18] F. D. M. Haldane, Phys. Rev. Lett. **61**, 2015 (1988).

[19] G. Jotzu, M. Messer, R. Desbuquois, M. Lebrat, T. Uehlinger, D. Greif, and T. Esslinger, Nature (London) **515**, 237 (2014).

[20] N. Fläschner, D. Vogel, M. Tarnowski, B. S. Rem, D. S. Lühmann, M. Heyl, J. C. Budich, L. Mathey, K. Sengstock, and C. Weitenberg, Nat. Phys. **14**, 265 (2018).

[21] X. L. Qi, Y. S. Wu, and S. C. Zhang, Phys. Rev. B **74**, 085308 (2006).

[22] H. C. Wu, L. Jin, and Z. Song, Phys. Rev. B **102**, 035145 (2020).

[23] M. C. Liang, Y. D. Wei, L. Zhang, X. J. Wang, H. Zhang, W. W. Wang, W. Qi, X. J. Liu, and X. B. Zhang, Phys. Rev. Res. **5**, L012006 (2023).

[24] M. Di Liberto, A. Recati, I. Carusotto, and C. Menotti, Phys. Rev. A **94**, 062704 (2016).

[25] C. F. Li, X. P. Li, and L. C. Wang, Europhys. Lett. **124**, 37003 (2018).

[26] L. H. Li, Z. H. Xu, and S. Chen, Phys. Rev. B **89**, 085111 (2014).

[27] L. Qi, Y. Yan, Y. Xing, X. D. Zhao, S. T. Liu, W. X. Cui, X. Han, S. Zhang, and H. F. Wang, Phys. Rev. Res. **3**, 023037 (2021).

[28] C. A. Li, Front. Phys. **10**, 861242 (2022).

[29] K. X. Hu, C. Chen, L. Qi, W. X. Cui, S. Zhang, and H. F. Wang, Phys. Rev. A **104**, 023707 (2021).

[30] X. Li, Y. X. Ma, D. J. Wang, Y. Wang, and S. C. Zhao, Phys. Rev. E **106**, 014124 (2022).

[31] M.-S. Wei, M.-J. Liao, C. Wang, C. J. Zhu, Y. P. Yang, and J. P. Xu, Opt. Express **31**, 3427 (2023).

[32] S. M. Young and C. L. Kane, Phys. Rev. Lett. **115**, 126803 (2015).

[33] M. C. Rechtsman, Y. Plotnik, J. M. Zeuner, D. H. Song, Z. G. Chen, A. Szameit, and M. Segev, Phys. Rev. Lett. **111**, 103901 (2013).
[34] A. V. Nalitov, D. D. Solnyshkov, and G. Malpuech, Phys. Rev. Lett. **114**, 116401 (2015).
[35] H. M. Guo, Y. Lin, and S. Q. Shen, Phys. Rev. B **90**, 085413 (2014).
[36] J. Ahn and B. J. Yang, Phys. Rev. Lett. **118**, 156401 (2017).
[37] K. Asaga and T. Fukui, Phys. Rev. B **102**, 155102 (2020).
[38] X. J. Luo, X. H. Pan, C. X. Liu, and X. Liu, Phys. Rev. B **107**, 045118 (2023).
[39] A. Götz, S. Beyl, M. Hohenadler, and F. F. Assaad, Phys. Rev. B **105**, 085151 (2022).
[40] Y. Otaki and T. Fukui, Phys. Rev. B **100**, 245108 (2019).
[41] X. Cai, Z. X. Li, and H. Yao, Phys. Rev. Lett. **127**, 247203 (2021).
[42] D. Y. Geng, H. Zhou, S. S. Yue, Z. Y. Sun, P. Cheng, L. Chen, S. Meng, K. H. Meng, and B. J. Feng, Nat. Commun. **13**, 7000 (2022).
[43] B. Xing, W. T. Chiu, D. Poletti, R. T. Scalettar, and G. Batrouni, Phys. Rev. Lett. **126**, 017601 (2021).
[44] H. Zhong, Y. V. Kartashov, Y. D. Li, and Y. Q. Zhang, Phys. Rev. A **107**, L021502 (2023).
[45] H. Y. Ma, Z. Zhang, P. H. Fu, J. S. Wu, and X. L. Yu, Phys. Rev. B **106**, 245109 (2022).
[46] M. C. Jin, Y. F. Gao, H. Z. Lin, Y. H. He, and M. Y. Chen, Phys. Rev. A **106**, 013510 (2022).
[47] H. Z. Wu, G. C. Wei, Z. Z. Liu, and J. J. Xiao, Opt. Lett. **46**, 4256 (2021).
[48] F. Liu, Phys. Rev. Lett. **118**, 076803 (2017).
[49] D. Obana, F. Liu, and K. Wakabayashi, Phys. Rev. B **100**, 075437 (2019).
[50] J. Cayssol and J. N. Fuchs, JPhys Mater. **4**, 034007 (2021).
[51] B. Pal, Phys. Rev. B **98**, 245116 (2018).
[52] Z. L. Gong, F. Y. Yang, and J. Yao, Phys. Rev. B **107**, L081404 (2023).
[53] C. Chen, L. Qi, K. X. Hu, J. Cao, W. X. Cui, S. Zhang, and H. F. Wang, Ann. Phys. **535**, 2200645 (2023).
[54] K. Kawabata, K. Shiozaki, M. Ueda, and M. Sato, Phys. Rev. X **9**, 041015 (2019).
[55] C. K. Chiu, J. C. Y. Teo, A. P. Schnyder, and S. Ryu, Rev. Mod. Phys. **88**, 035005 (2016).
[56] T. Liu, Y. R. Zhang, Q. Ai, Z. P. Gong, K. Kawabata, M. Ueda, and F. Nori, Phys. Rev. Lett. **122**, 076801 (2019).
[57] S. M. Rafi-Ul-Islam, Z. B. Siu, C. Sun, and M. B. A. Jalil, New J. Phys. **22**, 023025 (2020).
[58] S. M. Rafi-Ul-Islam, Z. B. Siu, and M. B. A. Jalil, Commun. Phys. **3**, 72 (2020).
[59] C. H. Lee, S. Imhof, C. Berger, F. Bayer, J. Brehm, L. W. Molenkamp, T. Kiessling, and R. Thomale, Commun. Phys. **1**, 39 (2018).
[60] N. A. Olekhno, E. I. Kretov, A. A. Stepanenko, P. A. Ivanova, V. V. Yaroshenko, E. M. Puhtina, D. S. Filonov, B. Cappello, L. Matekovits, and M. A. Gorlach, Nat. Commun. **11**, 1436 (2020).
[61] T. Helbig, T. Hofmann, C. H. Lee, R. Thomale, S. Imhof, L. W. Molenkamp, and T. Kiessling, Phys. Rev. B **99**, 161114(R) (2019).
[62] S. M. Rafi-Ul-Islam, Z. B. Siu, and M. B. A. Jalil, Appl. Phys. Lett. **116**, 111904 (2020).
[63] T. Hofmann, T. Helbig, C. H. Lee, M. Greiter, and R. Thomale, Phys. Rev. Lett. **122**, 247702 (2019).
[64] S. M. Rafi-Ul-Islam, Z. B. Siu, and M. B. A. Jalil, Phys. Rev. B **103**, 035420 (2021).
[65] Q. B. Zeng and R. Lü, Phys. Rev. B **104**, 064203 (2021).
[66] Q. B. Zeng and R. Lü, Phys. Rev. B **105**, 245407 (2022).
[67] D. Xiao, M. C. Chang, and Q. Niu, Rev. Mod. Phys. **82**, 1959 (2010).
[68] X. Ni, Z. Xiao, A. B. Khanikaev, and A. Alù, Phys. Rev. Appl. **13**, 064031 (2020).
[69] Y. H. Lu, N. Y. Jia, L. Su, C. Owens, G. Juzeliunas, D. I. Schuster, and J. Simon, Phys. Rev. B **99**, 020302(R) (2019).
[70] J. C. Bao, D. Y. Zou, W. X. Zhang, W. J. He, H. J. Sun, and X. D. Zhang, Phys. Rev. B **100**, 201406(R) (2019).